Published in "Journal of Electron Spectroscopy and Related Phenomena
doi: 10.1016/j.elspec.2012.09.001 , 2012"
which should be cited to refer to this work.

Photoinduced *K*-shell hollow atoms

J. Hoszowska*, J.-Cl. Dousse

Department of Physics, University of Fribourg, CH-1700 Fribourg, Switzerland

The mechanisms leading to the production of hollow *K* shell atoms via single photon impact were investigated for a variety of light elements with $12 \leq Z \leq 23$. The double 1*s* vacancy states were produced by irradiating the samples with intense monoenergetic synchrotron radiation beams. The double-to-single *K*-shell photoionization probabilities P_{KK} and the absolute double *K*-shell photoionization cross sections σ^{2+} were determined by measuring with a high-resolution bent von Hamos crystal spectrometer the $K\alpha^h$ hypersatellite X-ray emission of the samples. The measurements were performed over a wide range of incoming photon energies from threshold up to energies beyond the broad maximum of the double-to-single photoionization cross section ratios. The P_{KK} and σ^{2+} were determined from the relative yields of the resolved $K\alpha^h$ hypersatellite lines. For Mg, Al and Si, the two-electron one-photon (TEOP) $K\alpha\alpha^h$ transitions which represent an alternative but much weaker decay channel for double 1*s* vacancy states could be also observed, using a highly efficient flat crystal wavelength dispersive spectrometer. This observation of single photon-induced TEOP transitions has shown that the $I(K\alpha^h)/I(K\alpha\alpha^h)$ branching ratios are very poorly reproduced by most of existing theoretical models. Besides the relative yields of the hypersatellite and TEOP transitions, the energies and natural linewidths of the $K\alpha^h$ and $K\alpha\alpha^h$ X-ray lines were also determined. The energies are found to be in good agreement with different theoretical predictions, whereas the linewidths are significantly underestimated by the calculations, except if non-lifetime broadening effects such as the outer-shell ionization and the open valence configuration are taken into consideration.

1. Introduction

In the last years important efforts were undertaken by different experimental and theoretical groups to better understand the mechanisms involved in the production of *K*-shell hollow atoms via single photon impact and the subsequent radiative decay of the photoinduced double 1*s* vacancies. Hollow *K*-shell atoms are atoms that are characterized by an empty innermost shell and occupied outer shells. Since in photoabsorption or inelastic X-ray scattering processes, the incoming photon interacts with a single electron, the ejection of the two 1*s* electrons is driven by many-electron interactions. The latter playing a key role in the understanding of atomic structure (see [1,2] and references therein), single-photon double ionization processes have received a renewed interest in the last decade. The same holds for the decay of *K*-shell hollow atoms in which electron correlation effects do also play a crucial role.

As compared to atomic collisions involving heavy ions (HI), photoionization and inelastic X-ray scattering can be considered as soft collisions in a perturbation sense. As a consequence, rather pure *K*-shell hollow atoms are obtained, with no or only few additional vacancies in the outer shells, which makes the comparison with theoretical calculations easier and more reliable. On the other hand, the probability for creating double 1*s* vacancy states by single photon impact is quite low, ranging from a few percent for light elements down to about 10^{-5} for heavy ones. In this respect, experimental studies concerning hollow *K*-shell atoms have greatly benefited from the high intensity and energy tunability of synchrotron radiation sources. Furthermore, the recent advent of very intense hard X-ray free-electron laser (XFEL) beams permitting to investigate the dynamics of atomic electrons in the femtosecond time scale have given a new boost to the domain [3].

In single photon absorption, the creation of the second 1*s* vacancy is generally assumed to be due to two competitive mechanisms, namely the shake-off (SO) and knock-out (KO) processes that are both related to the ejection of the *K* photoelectron. In the SO process [4,5], the second 1*s* electron is excited into the continuum due to the sudden change of the atomic potential resulting from the fast removal of the primary electron. The SO probability is proportional to the squared overlap integral of the initial and final state wave functions of the shaken electron [6], provided the change of the atomic potential is much faster than the atomic relaxation time. In the KO process, the outgoing photoelectron knocks out the second 1*s* electron in an (e, $2e$)-like electron impact half-collision. Although the dependence of the two mechanisms on the

* Corresponding author. Tel.: +41 26 300 9210.
E-mail address: joanna.hoszowska@unifr.ch (J. Hoszowska).

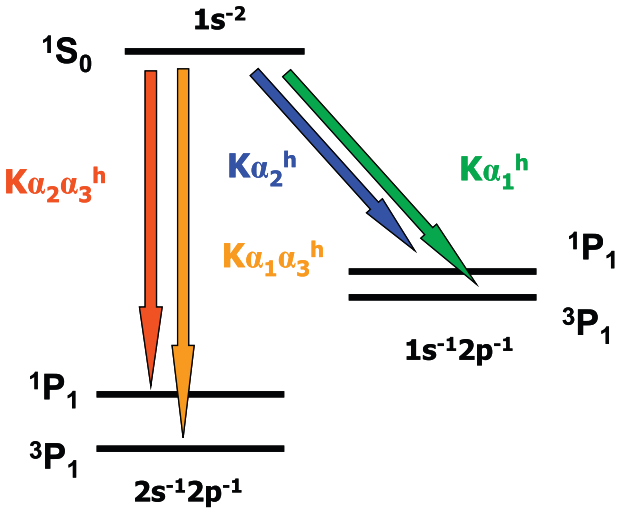

Fig. 1. Schematic of the TEOP (left) and OEOP (right) transitions.

incoming photon energy is very different, in most cases it is hard to distinguish the contributions of the two processes and attempts to separate them have given rise to intensive research [7–13].

Hollow *K*-shell atoms can be identified either by recording the *K* hypersatellite transitions in Auger electron spectra (*KK-KLL*, *KK-KLM*, etc.) or in X-ray fluorescence spectra (*KK-KL*; *KK-KM*, etc.). The most probable *K* hypersatellite transitions are those for which one of the two *K* vacancies is filled by a *L*-electron, namely *KK-KLX* (*X* = *L*, *M*, etc.) hypersatellites in Auger electron spectra and *KK-KL* (usually noted $K\alpha^h$) hypersatellites in X-ray fluorescence spectra. Auger spectroscopy is more likely used for light atoms because the fluorescence yields of the latter are low. However, this technique is limited to gaseous targets (see, e.g., [14]) or very thin solid samples, due to the strong absorption of low-energy electrons in matter. In addition the analysis of the measured hypersatellite Auger spectra is not easy because multiple Auger final states are possible. For these reasons, in the present study which concerns solid elements, the hollow *K*-shell atoms were investigated by means of high-resolution X-ray spectroscopy.

As shown in Fig. 1, the radiative decay of double 1*s* vacancy states may proceed through one-electron one-photon (OEOP) and two-electron one-photon (TEOP) transitions. The OEOP process, which corresponds to the $K\alpha^h$ ($1s^{-2} \rightarrow 1s^{-1}2p^{-1}$) hypersatellite transition represents to a large extent the predominant radiative decay channel of hollow *K*-shell atoms. In the TEOP $K\alpha\alpha^h$ ($1s^{-2} \rightarrow 2s^{-1}2p^{-1}$) transition, the two *K*-shell core holes are filled simultaneously via a correlated two-electron jump and a single photon having an energy which is approximately twice that of the parent $K\alpha$ diagram line is emitted. Despite their extremely weak intensities as compared to those of hypersatellites, TEOP transitions are of interest because they correspond to correlated multielectron processes.

The theoretical prediction of TEOP transitions dates back to 1925 [15] but the first experimental evidence for this correlated two-electron decay channel was reported only about 50 years later [16]. Actually, this first observation was done somewhat accidentally while analyzing a HI-induced *K* X-ray spectrum, in which a very weak X-ray line having the same energy as the one of the TEOP transition was found. The $K\alpha^h$ to $K\alpha\alpha^h$ branching ratio is not expected to depend on the excitation mode. However, multiple electron ionization in HI collisions change the electronic configurations and affect the intensities and energies of the measured transitions. Thus data from HI collision experiments show a wide spread of values [17–21], making comparison with theory often inconclusive. In this respect, photon impact data provide more reliable results and a more stringent test for atomic structure calculations. In counterpart, single-photon double *K*-shell ionization cross sections are 10^2–10^3 smaller than in HI collisions. Thus photoionization experiments are more challenging and, to the best of our knowledge, all attempts to measure photoinduced TEOP transitions have been unsuccessful (see e.g., [22]) until very recently [23]. Note that the TEOP analogous *KK-LLX* (*X* = *L*, *M*, etc.) three-electron Auger transitions corresponding to the simultaneous filling of the two *K* vacancies by the correlated jump of two *L*-electrons and the transfer of the entire transition energy on the Auger electron *X* have never been observed so far. However, similar three-electron Auger transitions of the type *LL-MMM* could be detected in Ar as a result of low-energy collisions with several heavy ions [24].

In this paper we present an overview of the experimental and theoretical efforts done in the last decade in the endeavor of bringing new insights to electron–electron interactions and in understanding the double photoionization in many-body systems. In particular, the photon energy evolution of the double-to-single photoionization cross section ratios for several light elements with $12 \leq Z \leq 23$ are reported for a wide photon energy range. The *Z*-dependent trends and scaling properties of these ratios and the double photoionization (DPI) cross sections are examined. The energies and linewidths of the $K\alpha^h$ hypersatellite X-ray transitions and the $K\alpha_1^h/K\alpha_2^h$ intensity ratios are reported and compared to theoretical calculations as well as to other available experimental data. For Mg, Al and Si, the correlated two-electron one-photon transitions in single-photon *K*-shell double ionization could be observed recently for the first time [23]. The TEOP energies and $K\alpha^h$ to $K\alpha\alpha^h$ branching ratios obtained in this experiment are also presented and discussed.

2. Experimental method

In X-ray spectroscopy the *K* hypersatellite lines can be either observed directly with high resolution wavelength-dispersive spectrometers or indirectly by measuring in coincidence the emitted $K\alpha^h$ hypersatellite and subsequent $K\alpha L$ satellite X-rays, using two energy-dispersive detectors. The coincidence technique [12] is preferable to high resolution X-ray spectroscopy in case of heavy elements for which the $K\alpha^h$ hypersatellites lie on the high-energy tails of the $\sim 10^5$ stronger parent $K\alpha$ diagram lines. The disadvantage of the coincidence method is that, due to the poor resolution of the energy-dispersive detectors, only the ratio of double to single *K*-shell ionization cross sections can be extracted accurately and not the energy of the hypersatellite transitions, nor their natural width. Many wavelength dispersive spectrometers have been designed and constructed in the last years. For soft and tender X-rays, Bragg-type crystal spectrometers are usually employed. Setups based on cylindrically or spherically bent crystals or arrays of crystals arranged in the Johann [25–27], Johansson [28] or von Hamos geometry [29,30] and setups using flat crystals combined with half-lense polycapillary X-ray optics [31] were developed. Most of these crystal spectrometers were optimized for specific techniques such as resonant inelastic X-ray scattering (RIXS), high energy resolution fluorescence detected X-ray absorption spectroscopy (HERFD-XAS) and X-ray Raman spectroscopy (XRS) applied to solid, liquid and gaseous samples. To a smaller extent, more versatile and transportable instruments designed for the high-resolution measurement of the X-ray fluorescence resulting from the atomic core-levels' excitation by impact with photons, light charged particles and heavy ions were also developed [29,28].

The experiments discussed in the present paper were performed at the European Synchrotron Radiation Facility (ESRF), using intense, monochromatic and energy-tunable synchrotron radiation beams to produce the double 1*s* vacancy states in a variety

of light elements (Mg, Al, Si, Cl, K, Ca, Sc and V). To probe the evolution of the double-to-single photoionization cross-section ratios over wide photon beam energy ranges up to ~3 times the DPI threshold energies, the measurements of the *K* hypersatellite and diagram X-ray transitions were carried out at two undulator beamlines (ID21 and ID26), and at a bending magnet beamline (BM5). The measurements were performed by means of high-resolution X-ray spectroscopy, using for all measurements except the TEOP ones the Fribourg von Hamos Bragg-type curved crystal spectrometer [29,32]. High-energy resolution was mandatory because the Mg, Al and Si *K* hypersatellites are partly or completely overlapping with the *L*-satellites of the diagram $K\beta$ ($1s^{-1} \rightarrow 3p^{-1}$) lines, and in the case of Cl, K, and Ca the $K\alpha$ hypersatellites need to be resolved from the close lying *KMM* radiative Auger transitions [33,34].

The principal elements of the von Hamos spectrometer of Fribourg are an effective X-ray source, a crystal bent cylindrically to a nominal radius of 25.4 cm, and a position-sensitive detector, located on the crystal axis of curvature. The von Hamos geometry permits at one positioning of the elements, data collection over an energy bandwidth limited primarily by the detector length. The effective X-ray fluorescence source viewed by the crystal is usually defined by a rectangular slit with an adjustable width. Alternatively, the effective source size may be defined by a focused beam spot on the sample, and the slit is left wide open. This so-called slit-less operation mode results in a higher overall detection efficiency. The sample, crystal and detector are all contained in an evacuated stainless steel chamber. In the present experiments the von Hamos spectrometer was equipped with four different crystals, namely a TlAP(0 0 1) ($2d$ = 25.772 Å), an ADP(1 0 1) ($2d$ = 10.642 Å), a LiF(2 0 0) ($2d$ = 4.028 Å), and a Ge(2 0 0) ($2d$ = 4.000 Å) crystal. The diffracted X-rays were recorded with a thermoelectrically cooled (−45 to −50 °C) back-illuminated charge coupled device (CCD) camera consisting of 1340 columns and 400 rows with a pixel size of 20 μm × 20 μm. By setting appropriate energy windows, the CCD detector allows discrimination against higher-order crystal reflections and also a rejection of background events.

At the beamline ID21 where the Mg and Al measurements were performed the von Hamos spectrometer was installed downstream of the Scanning Transmission X-ray Microscope (STXM) chamber. Monochromatic photon beams ranging from 2.7 to 8.0 keV for Mg and from 3.1 to 7.0 keV for Al with ~10 eV bandwidth were obtained using the double Ni/B_4C multilayer monochromator. For upper harmonics rejection, a Ni-coated mirror was employed. The beam size was defined by means of a 1 mm in diameter pinhole. For the measurements of Cl, K, Ca and V, the spectrometer was installed at the BM5 beamline, in the first experimental hutch. The primary X-ray beam was monochromatized by means of a $[Ru/B_4C]_{70}$ double-multilayer monochromator with an energy resolution $\Delta E/E$ of $\sim 2 \times 10^{-2}$ and an harmonics rejection rate of 1.8×10^{-4} in the 6–30 keV photon energy range. The beam size on the sample was defined by means of a 2 mm high and 5 mm wide rectangular slit placed in front of the spectrometer beam port. The Si and Sc X-ray spectra as well as data at higher beam energies for Mg, Al, Ca and V were collected at the beamline ID26. For photon energies up to 16 keV the Si(1 1 1) double-crystal monochromator was employed, whereas for higher energies the Si(3 1 1) monochromator was used. Depending on the photon energy, double Si, Cr- and Pd-coated, and double Pt-coated mirrors suppressed the upper harmonics, and for incident beam energies in the 3–5 keV range the monochromator crystals were additionally detuned. The upper harmonics rejection efficiency was $\sim 10^{-4}$–10^{-5}. The mirrors served also to focus the beam horizontally on the sample to ~250 μm, permitting thereby to operate the spectrometer in the slit-less geometry.

The incident photon flux was ~ 1–3×10^{12} ph/s at the three beamlines. The exposure time of the CCD was chosen depending on the count rate. For the diagram X-ray transitions, acquisition times of 1 s per image were chosen, and to avoid multiple-hit events on one pixel the incoming photon fluxes were attenuated with appropriate absorbers. The hypersatellite X-ray spectra were collected in short successive scans of few hundred CCD images with acquisition times of 2–10 s per image. For the X-ray hypersatellite spectra of Cl, K and Ca, two or three overlapping CCD regions were measured to include the *KMM* radiative Auger transitions and $K\beta$ diagram lines. For normalization purposes, the number of incoming photons was determined with a photo-diode at the beginning and the end of each X-ray emission spectrum measurement. This allowed to monitor the photon flux and to correct the X-ray spectra off-line for any beam intensity fluctuations.

The TEOP measurements were performed at the beamline ID21, using the wavelength dispersive spectrometer (WDS) [31] which was installed recently at the Scanning Transmission X-ray Microscope (STXM) chamber. The WDS consists mainly of a polycapillary optics for the collection of the sample X-ray fluorescence, a flat crystal and a flow gas X-ray detector. Due to the ultra low intensities of the TEOP transitions and the presence of stronger diagram X-ray lines from trace impurities in the measured spectra, high-efficiency and good energy resolution were indeed prerequisite for this challenging experiment. For the Mg and Al measurements, the WDS spectrometer was equipped with a Si(1 1 1) crystal ($2d$ = 6.271 Å), whereas for the Si ones a Ge(2 2 0) crystal ($2d$ = 4.000 Å) was employed. The energy calibration of the WDS was determined from measurements of several diagram transitions (Rh, Ru, Cl, Pd, Ag, Sn, K, and Sc), using for the energies of the reference transitions the values reported in [35]. These measurements also served to determine the full width at half maximum (FWHM) of the Gaussian instrumental response function. The FWHM was found to vary, depending on the energy, between 7 and 10 eV.

In order to obtain the highest possible flux on the samples, the SR from two undulators was used. The intense beam was monochromatized using the double Ni/B_4C multilayer monochromator and focused on the samples with a Kirkpatrick–Baez optics for Al and Si, and polycapillary optics for Mg. Upper harmonics were rejected by means of Ni-coated mirrors set to an angle of 7.5 mrad. The microfocused incident photon flux was ~ 2–3.5×10^{12} photons/s. Photon beam energies of 3.364 keV for Mg and 4.620 keV for Al and Si were employed to produce the sample fluorescence. These energies were chosen to match the *K*-shell double photoionization cross-section maxima reported in [2]. Self-supported metallic foils of Mg, Al, and a c-Si were employed. The Al and Si sample purity was 99.999%, and that of Mg 99.9%. The X-ray spectra were collected in successive scans of ~0.5–1 h each, with total acquisition times of ~42 h, ~51 h, and ~17 h, for Mg, Al and Si, respectively. For normalization purposes the photon flux was recorded with a photo-diode at the beginning and the end of each scan.

Since for all three elements it was not possible to measure with the same crystal the hypersatellite and TEOP transitions, the branching ratios $I(K\alpha^h)/I(K\alpha\alpha^h)$ were derived from the measured intensity ratios between the TEOP and close-lying reference *K* X-ray diagram transitions. This approach benefited from well known values of the single [37] and the double [2] *K*-shell photoionization cross sections and presented the additional advantage to minimize the corrections related to the energy dependent polycapillary transmission.

3. Results and discussion

3.1. Double K-shell photoionization

3.1.1. Double-to-single photoionization cross section ratios

The double-to-single photoionization cross section ratios P_{KK} were obtained from the relative intensities of the resolved

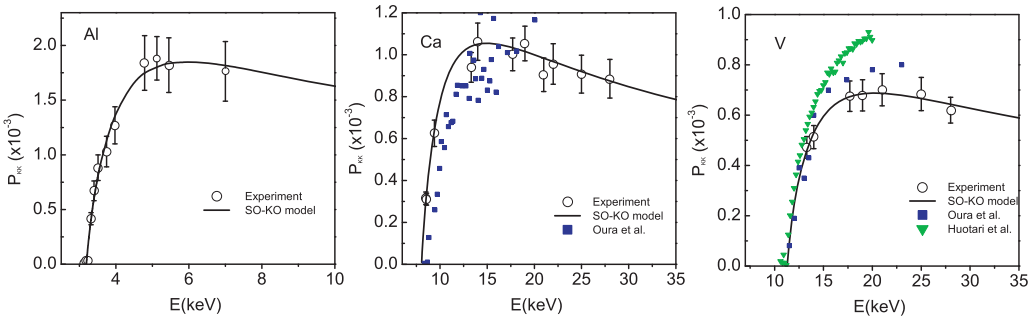

Fig. 2. Double-to-single *K*-shell photoionization ratios P_{KK} for Al, Ca, and V versus the photon beam energy. For Ca and V the present experimental data are compared to those of Oura et al. [38] and Huotari et al. [13]. The solid black lines correspond to the best fits to our data with the SO–KO empirical model.

hypersatellite $K\alpha^h$ ($1s^{-2} \rightarrow 1s^{-1}2p^{-1}$) to the diagram $K\alpha$ ($1s^{-1} \rightarrow 2p^{-1}$) X-ray transitions:

$$P_{KK} = \frac{I_{K\alpha^h}}{I_{K\alpha}} \frac{\omega_K}{\omega_{KK}}, \tag{1}$$

where ω_K and ω_{KK} are the fluorescence yields for the single- and double-hole states [36], respectively. The evolution of the double *K*-shell photoionization ratios P_{KK} with the photon energy for selected elements is presented in Fig. 2. It should be pointed out, that in contrast to *L*-shell X-ray satellite lines, the *M*-satellites cannot be resolved, their energy shift being smaller than the natural linewidths of the parent diagram or hypersatellite lines. The intensities of these *M*-satellites are therefore included in the measured $I_{K\alpha}$ and $I_{K\alpha^h}$ yields. As the *M*-shell shake probability is expected to be higher for atoms with a double 1*s* vacancy in the initial state than for those with a single 1*s* vacancy, the P_{KK} ratios calculated with Eq. (1) might be somewhat overestimated. However, there is no experimental evidence that the *K*-shell shake or the knock-out process takes place prior to the *M*-shell shake, and in first approximation it is reasonable to consider the production of the second 1*s* vacancy and the *M*-shell vacancy as quasi-simultaneous. We are therefore inclined to believe that the systematic error related to the difference in the *M*-shell shake probabilities resulting from the single and double *K*-shell photoionization is small in our case. This assumption seems to be confirmed by the fact that, despite a very good instrumental resolution, no asymmetry was observed in the fitted hypersatellite transitions, indicating that the contamination of the hypersatellite transitions by unresolved *M*-satellite was weak for the measured elements.

Because the photon interacts with only one electron and vanishes, in single-photon *K*-shell double photoionization the removal of the two innermost electrons producing a *K*-shell hollow atom is due to electron correlations. Two mechanisms dominate the *K*-shell double photoionization, namely, the shake-off (SO) process [39] and the inelastic electron–electron scattering (knock-out). These electron–electron interactions are of quantum and classical nature. The double *K*-shell photoionization via shake is a consequence of the change of the self-consistent field and electron–electron correlations [39]. In the knock-out (KO) the outgoing photoelectron knocks out the second 1*s* electron in an (*e*,2*e*)-like electron impact half-collision [40]. Further, ground-state electron correlations are important for the shake-off, whilst the final-state electron interactions govern the dielectronic process. Although qualitatively the two mechanisms have very different photon energy dependences and different electron interaction times, the separation of KO and SO and quantification of the interferences is not straightforward (see e.g., [7,10,41,42,11,43]). In comparison to He and He-like ions, much less theoretical effort has been devoted to the DPI of neutral atoms. The single-photon *K*-shell DPI was addressed within the lowest order perturbation theory [11], and a first systematic study using an *ab initio* nonperturbative close-coupling approach was performed by Kheifets et al. [42] showing difficulties of such a calculation which is particularly demanding to the accuracy of the ground state wave-function. In contrast to *ab initio* approaches in which the SO and KO are treated coherently, alternative theoretical models based on an incoherent picture of the (*e*,2*e*)-like process and shake-off were proposed by Samson [44] and elaborated by Pattard and Burgdörfer [45]. A theoretical model for an incoherent separation of SO and KO was also developed by Schneider et al. [8,9]. The latter is based on a quasi-classical formulation of the KO and the purely quantum mechanical nature of SO, i.e., SO is viewed as a quantum correction to the quasi-classically calculated double photoionization. For He, an excellent agreement with the experimental data was obtained, suggesting that interferences play only a minor role.

In the same spirit, to assess the effect of outer shell electrons and the relative importance of initial-state and final-state electron–electron correlations to the *K*-shell DPI, an empirical SO–KO model based on an incoherent summation of the double-to-single cross section ratios for the shake process and knock-out was proposed [1,2]. In our SO–KO model the double-to-single photoionization ratio as a function of the photon energy is given by:

$$P_{KK}(E) = P_{\mathrm{SO}}(E) + P_{\mathrm{KO}}(E), \tag{2}$$

with

$$P_{\mathrm{SO}}(E) = R_\infty \exp\left[-\frac{(rE^+)^2}{15.32(E-E^{2+})}\right] \tag{3a}$$

and

$$P_{\mathrm{KO}}(E) = P_{\mathrm{KO}}^{max}\left[\cosh\left(\beta \ln\left[\frac{E-E^{2+}}{\Delta E_{\mathrm{KO}}^{max}}\right]\right)\right]^{-1/\beta}. \tag{3b}$$

The $P_{\mathrm{SO}}(E)$ corresponds to the expression of Thomas [46] for shake-off. R_∞ stands for the shake-off asymptotic high-energy limit, i.e., when the photoelectron is infinitely fast, E^+ is the binding energy of the remaining *K*-shell electron, r represents the distance in Å traveled by the *K* photoelectron during the time the atomic potential changes, and E^{2+} denotes the DPI threshold energy. All energies are in eV. Because the shake-off asymptotic non-relativistic high-energy limit can be calculated quite accurately for the helium isoelectronic sequence and it is almost the same for neutral atoms and He-like ions [42,47], for R_∞ the values from Forrey et al. [48] were used. For the knock-out probability $P_{\mathrm{KO}}(E)$, the analytical form of the universal shape function for electron impact ionization of H-like ions of Aichele et al. [49] was adopted. The choice of the shape function was based on the similarity of electron-impact ionization of a H-like ion to the KO part of the double photoionization of the corresponding He-like ion [44,10,9,45]. The P_{KO}^{max} corresponds to the maximum value of KO, $\Delta E_{\mathrm{KO}}^{max}$ to the excess energy where the maximum occurs, and the power $\beta = 0.4$.

Table 1
Double-to-single photoionization cross section ratios in the peak region of the photon energy evolution P_{KK}^{max} and the fitting parameters of the SO–KO model. The DPI threshold energy E^{2+} and the P_{KO}^{max} were derived from the fits, while E^{+} values and the photoabsorption asymptotic limits R_{∞} were kept fixed. The effective nuclear charge Z^{*} was deduced using the hydrogenic formula $E^{+}=Z^{*2}$Ry, where Ry = 13.6 eV. Listed are also the MCDF predictions for the DPI threshold energy E_{MCDF}^{2+}. The ω_{KK}/ω_{K} were deduced from the values quoted by Chen [36]. Note, that for Cl and K the X-ray emission spectra were collected at a single photon energy of 13.3 keV in the region of the broad maximum of the double-to-single photoionization cross-section ratios. The obtained P_{KK}^{max} is 8.61(1.77)×10^{-4} for Cl, and 9.24(1.23)×10^{-4} for K.

Element	Z	Z^{*}	P_{KK}^{max}	ω_{KK}/ω_{K}	E^{2+} (eV)	E_{MCDF}^{2+} (eV)	E^{+} (eV)	R_{∞}	P_{KO}^{max}
Mg	12	10.4	2.03(19)×10^{-3}	1.27	2741(35)	2776.6	1464.8	6.08×10^{-4}	1.74×10^{-3}
Al	13	11.3	1.83(20)×10^{-3}	1.24	3189(23)	3294.0	1736.8	5.20×10^{-4}	1.55×10^{-3}
Si	14	12.2	1.43(14)×10^{-3}	1.21	3788(42)	3882.5	2032.5	4.47×10^{-4}	1.20×10^{-3}
Ca	20	17.8	1.02(10)×10^{-3}	1.08	8039(40)	8357.0	4324.7	2.22×10^{-4}	9.42×10^{-4}
Sc	21	18.8	7.84(74)×10^{-4}	1.075	9060(53)	9297.4	4791.8	2.00×10^{-4}	6.60×10^{-4}
V	23	20.7	6.87(63)×10^{-4}	1.065	11,277(110)	11283.1	5798.7	1.68×10^{-4}	6.10×10^{-4}

The best fits to the double-to-single photoionization ratios of Mg, Si and Sc as a function of the scaled excess energy are depicted in Fig. 3 and results of the least-squares fits to the experimental data with Eq. (2) are listed in Table 1. On inspection of Fig. 3 the prevalence of KO near threshold and for intermediate excess energies can be observed. At high excess energies KO becomes negligible and the P_{KK} ratios approach the SO photoabsorption asymptotic limit. These results are in accord with the conclusions of Kanter et al. [12] and Huotari et al. [13] for the prevalence of KO in the near-threshold region and for intermediate photon energies of the P_{KK} photon energy evolution. The very good agreement between the experimental data for the photon energy dependence of P_{KK} and the SO–KO model fit supports this physical picture for the K-shell double photoionization for low-Z neutral atoms.

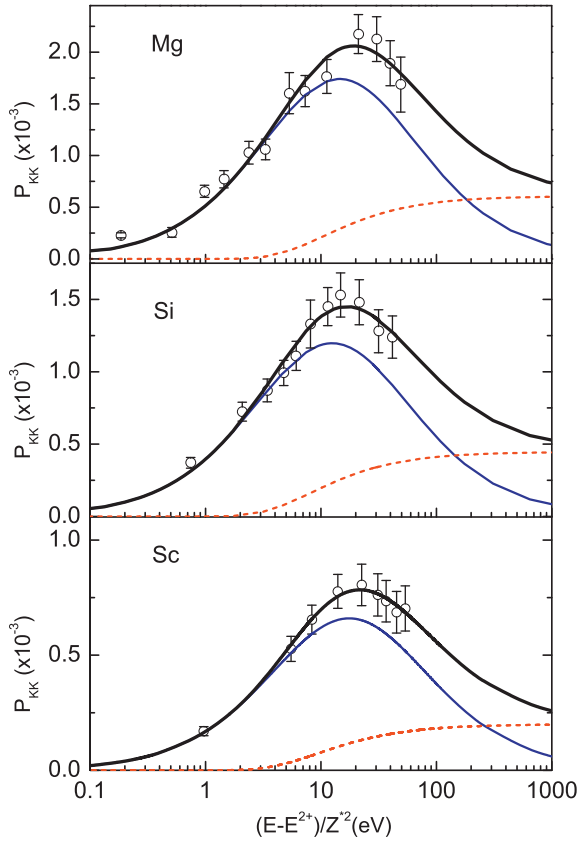

Fig. 3. Double-to-single K-shell photoionization ratios as a function of the scaled excess energy. For E^{2+} values from the fit were used. Results of best fits to our data with the SO–KO empirical model are represented by black solid thick lines, whereas the KO contributions are depicted by thin blue lines and the SO by red dashed lines. (For interpretation of the references to color in this figure legend, the reader is referred to the web version of the article.)

3.1.2. Double-photoionization cross sections

The experimental double K-shell photoionization cross sections σ^{2+} as a function of the photon energy are depicted in Fig. 4. The values were determined employing the relation

$$\sigma^{2+}(E) = P_{KK}(E)\sigma^{+}(E), \tag{4}$$

where E is the photon energy and σ^{+} stands for the single K-shell photoionization cross section deduced from the XCOM database [37]. For all elements the cross sections show a common shape characterized by a sharp rise above the threshold for double ionization to the maximum and a subsequent rapid decrease with the photon energy. Pattard [50] established an universal shape function for multiple ionization by photons that provides an excellent parameterization of photoionization cross sections for double ionization of He-like ions. The analytical formula reads:

$$\sigma^{2+}(\Delta E) = \sigma_{max}^{2+} x^{\alpha}\left[\frac{\alpha+7/2}{\alpha x+7/2}\right]^{(\alpha+7/2)}, \tag{5}$$

where σ_{max}^{2+} denotes the cross section maximum, $\alpha = 1.056$, and $x = \Delta E/\Delta E^{max}$. ΔE and ΔE^{max} correspond to excess energies. Least-squares fits to the experimental data with Eq. (5) demonstrate that the shape function is applicable to K-shell hollow atoms as well (see Fig. 4). The photon energies and the excess energies corresponding to the DPI cross section maxima scale as $E^{max}(Z^{*}) = 25.03(11)Z^{*2.08(3)}$ and $\Delta E^{max}(Z^{*}) = 5.72(0.07)Z^{*2.00(7)}$, respectively. A power-law fit to the maximum values of σ^{2+} as a function of effective nuclear charge Z^{*} yields a $0.15(5)/Z^{*3.68(11)}$ fall-off. Further, as shown in Fig. 5, the double photoionization cross sections in the range $2 \le Z \le 47$ exhibit an universal scaling behavior in reduced coordinates $\sigma^{2+}Z^{*3.68}$ against $(E-E^{2+})/Z^{*2}$ and coincide with the $\sigma^{2+}Z^{*4}$ for the He isoelectronic series [1,2].

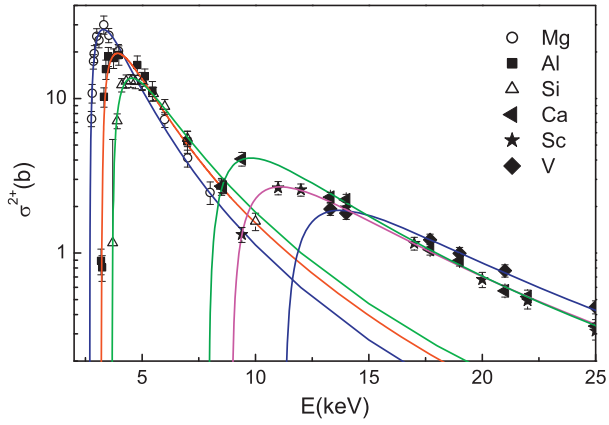

Fig. 4. Double K-shell photoionization cross-sections versus the photon energy. Solid lines show the best fits with the universal shape function of Pattard [50].

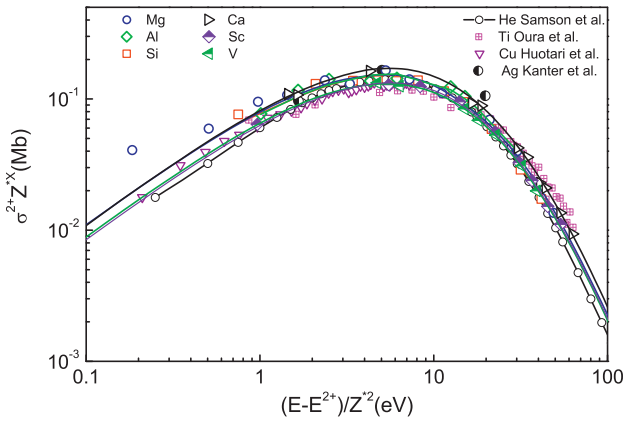

Fig. 5. Scaled experimental DPI cross sections for Mg, Al, Si, Ca, Sc and V compared to the scaled data for He [40] and experimental data for Ti [38], Cu [13] and Ag [12] as a function of the scaled excess energy. For neutral atoms the scaling exponent X is 3.68. The curves (solid lines) were deduced from the results of the best fits of P_{KK} with the SO–KO model.

3.2. Radiative decay of double K-shell hole states

3.2.1. One-electron one-photon and two-electron one-photon X-ray transitions

Following the K-shell DPI, the atomic doubly-excited core state decays in a cascade of non-radiative Auger and radiative transitions. The radiative de-excitation of K-shell double hole states via the one-electron-one-photon process corresponding to the $K\alpha^h(1s^{-2}\rightarrow 1s^{-1}2p^{-1})$ hypersatellite transition is the main decay channel. De-excitation through transitions from other subshells is also possible, but less probable. The alternative decay channel TEOP in which the two K-shell core-holes are filled simultaneously via a correlated two-electron jump of one $2s$ and one $2p$ electron and one photon is emitted $K\alpha\alpha^h(1s^{-2}\rightarrow 2s^{-1}2p^{-1})$ is even few orders of magnitude weaker.

These transitions permit not only to investigate the double ionization process, but also give insight in fundamental aspects of atomic physics as Breit interaction, quantum electrodynamics (QED) and relativity effects. Since the $K\alpha_1^h$ hypersatellite originates from the spin-flip transition ($^3P_1\rightarrow{}^1S_0$) which is dipole forbidden in the pure L–S-coupling scheme, the $I_{K\alpha_1^h}/I_{K\alpha_2^h}$ intensity ratio probes the intermediacy of the coupling scheme across the periodic table and the various effects that influence the mixing, for instance Breit interaction and relativity. In fact, the TEOP transitions are even more sensitive to the Breit interaction than the hypersatellites. Of interest are also the radiative linewidths which are related to the mean lifetimes of the doubly-excited states by the Heisenberg uncertainty relation $\Gamma\tau=\hbar$, where Γ is the width and τ is the lifetime of an excited atomic state. Further, as the TEOP transitions are correlated multi-electron processes they can be only described by many-electron models. Thus, both the OEOP and TOEP radiative transitions provide a stringent test for the multi-configuration calculations.

For illustration, the OEOP and TEOP X-ray emission spectra of Mg, Al and Si are shown in Fig. 6. Due to the change in the electronic screening of the nuclear charge, the energies of the OEOP transitions are shifted with respect to their parent X-ray lines decaying singly-ionized states. Although for Mg and Al the $K\alpha_1^h$ X-ray transition was much too weak to be observed, it was measured for the first time for Si. The obtained $E_{K\alpha_1^h}$ and $K\alpha_2^h$ hypersatellite and $E_{K\alpha\alpha_2^h}$ TEOP energies are summarized in Table 2 and compared to the few existing data and the most recent theoretical calculations from Martins et al. [52], Costa et al. [51], Natarajan [53] and Saha et al. [56]. The energies of the $K\alpha_2^h$ and $K\alpha\alpha_2^h$ transitions for lower Z elements are in good to very good agreement within the experimental uncertainties with different theoretical predictions. At higher Z, theory underestimates the experimental energies for both the $K\alpha_2^h$ and $K\alpha_1^h$ lines, and the differences are found to be greater for the $K\alpha_1^h$ hypersatellites.

The $I_{K\alpha_1^h}/I_{K\alpha_2^h}$ intensity ratios are listed in Table 3. For Si, the experimental ratio was found to be in excellent agreement with the MCDF theoretical predictions of Costa et al. [51] that include both the Breit and QED contributions. Indeed, these calculations predict that for elements $Z<18$ the intensity ratio of the hypersatellite lines does not follow the same regular trend as that observed for $Z\geq 18$, but peaks at $Z=15$. This effect is interpreted as being due to the interaction between the hole in the $2p$ level and the $3p$ electrons that opens several decay channels and leads to an increase of the $I_{K\alpha_1^h}/I_{K\alpha_2^h}$ intensity ratio. For Ca and Sc our data compare well within the experimental uncertainties with theory [51], but in the case of V the calculations overestimate our result. The present ratio for V, however, agrees very closely with the experimental and the relativistic MCDF-calculated values reported by Diamant et al. [59].

The finite lifetime τ gives to an X-ray transition line a Lorentzian shape with a natural width equal to the sum of the total radiative and non-radiative widths of the initial and final states involved in

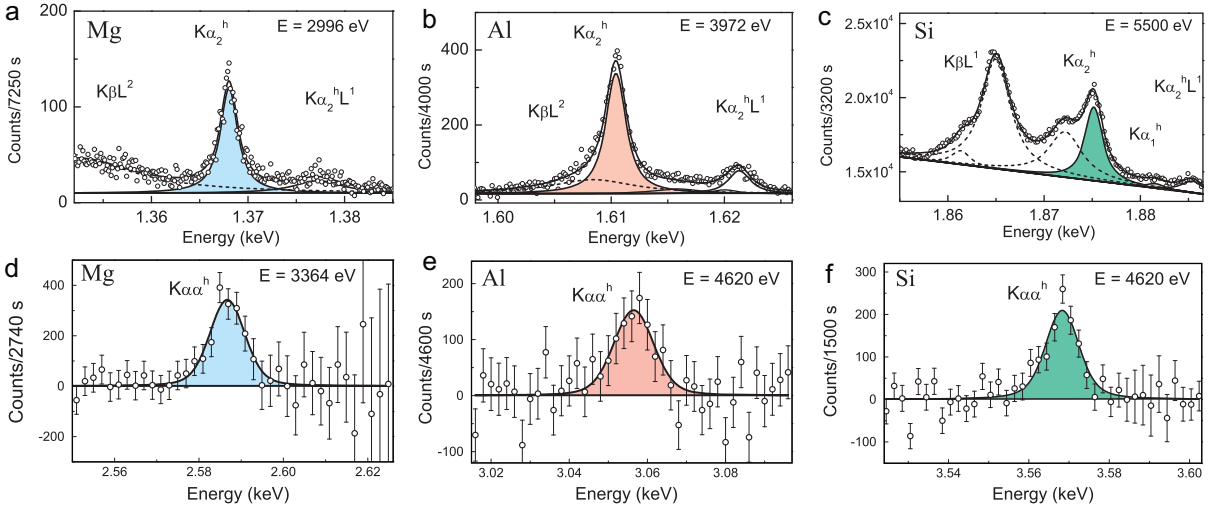

Fig. 6. One-electron one-photon (upper panels) and two-electron one-photon (lower panels) transitions of Mg, Al and Si. The TEOP spectra correspond to residuals of the measured data sets. The solid lines are the best least-squares fits to the data using Voigt functions.

Table 2
Energies of the one-electron-one-photon and two-electron-one-photon transitions compared to other experimental data and theoretical predictions. Since Costa et al. [51] present energy shifts relative to the corresponding diagram lines, the listed $K\alpha_1^h$ and $K\alpha_2^h$ transition energies were calculated using the recommended values of Deslattes et al. [35] for the $K\alpha_1$ and $K\alpha_2$ lines. The notation 1367.86(9/6) means 1367.86 ± 0.09 eV with an included statistical error from the fit of 0.06 eV.

Z	$K\alpha_2^h$(eV)				$K\alpha_1^h$(eV)				$K\alpha\alpha_2^h$(eV)	
	Experiment	Theory			Experiment	Theory			Experiment	Theory
		[52]	[51]	[53]		[52]	[51]	[53]		
12	1367.86(9/6) 1367.8(2) [54] 1367.7(6) [55]	1368.53	1367.71	1367.7					2586.7(4)	2585.45 [52]
13	1610.38(4/2)	1611.75	1610.89						3056.5(9)	3056.54 [52] 3057.49 [56] 3058.68 [57] 3055.99 [57][a]
14	1874.87(6/4) 1873.6(1) [58]	1874	1873.99	1874.5	1881.20(12/8)	1880	1879.96	1881.6	3568.3(4)	3566 [52] 3567.43 [56] 3569.37 [57]
17	2787.80(10/8)	2785								
19	3499.20(9/6)	3498	3497.77							
20	3887.50(9/5) 3883.5(6) [58]	3884.8	3885.93	3884.5	3899.80(15/9)	3896.39	3897.54	3896.3		
21	4296.31(8/7)	4294.16	4295.24		4309.6(7/6)	4306.27	4307.43			
23	5177.65(8/6) 5178.1(5) [38] 5176.6(1) [59]	5174	5176.24		5192.0(9/7) 5191.7(1) [59]	5188	5190.86			

[a] $K\alpha\alpha^h$ rates include the coupling of the initial and final state vacancies with the 3*p* electron.

Table 3
Linewidths of the one-electron one-photon and two-electron one-photon transitions, and the $I_{K\alpha_1^h}/I_{K\alpha_2^h}$ intensity ratios. The $\Gamma_{K\alpha_1^h}$ for Si, Ca and Sc were fixed in the spectra fits.

Z	$\Gamma_{K\alpha_2^h}$ (eV)	$\Gamma_{K\alpha_1^h}$ (eV)	$\Gamma_{K\alpha\alpha_2^h}$ (eV)	$I_{K\alpha_1^h}/I_{K\alpha_2^h}$	
				Exp.	[51]
12	1.49(8)		2.5(6)		0.00074
13	1.88(7)		2.9(1.7)		0.0087
14	1.86(9)	1.86	3.8(9)	0.03(1)	0.0288
17	2.86(34)				
19	3.46(22)				0.0189
20	3.72(18)	3.72		0.035(13)	0.0274
21	3.88(17)	3.75		0.045(9)	0.051
23	5.54(19) 5.5(1) [59]	5.6(1.0) 6.0(6) [59]		0.077(15) 0.08(1) [59]	0.0989

the transition. The linewidths of the OEOP and TEOP transitions can be thus approximated by the sum of the total atomic level widths of the initial $1s^{-2}$ and final double-hole configuration states $1s^{-1}2p^{-1}$ and $2s^{-1}2p^{-1}$, respectively:

$$\Gamma_{K\alpha^h} \simeq \Gamma_{KK} + (\Gamma_{KL_{2,3}^{-1}} + \Gamma_{L_{2,3}}) \quad (6)$$

and

$$\Gamma_{K\alpha\alpha^h} \simeq \Gamma_{KK} + (\Gamma_{L_1} + \Gamma_{L_{2,3}}), \quad (7)$$

where Γ_{KK} is the double-*K* hole state width [36,53], Γ_L is the single-*L* hole state width, and $\Gamma_{KL_{2,3}^{-1}}$ is the reduced *K* level width due to the presence of the *L*-shell spectator vacancy [62,63,58].

Present experimental $\Gamma_{K\alpha^h}$ and $\Gamma_{K\alpha\alpha^h}$ linewidths are summarized in Table 3, and in Fig. 7 the $\Gamma_{K\alpha_2^h}$ values are compared to those calculated using Eq. (6) and theoretical predictions of Polasik et al. [60]. The single- and double-vacancy level widths and other experimental data are also shown. The widths Γ_{KK} and Γ_K were obtained by interpolating the values corresponding to the atomic numbers selected by Chen [36]. The accuracy of the interpolation procedure is at the level of ~1–4%. The $\Gamma_{KL^{-1}}$ widths were estimated following the scaling procedure of Larkins [62] and using for the radiative and Auger *K* level widths the interpolated values from Chen [36]. For the Γ_L, the recommended values of Campbell and Papp [61] were adopted.

From Fig. 7 it can be seen that for elements in the $12 \le Z \le 30$ range the $\Gamma_{K\alpha^h}$ linewidths calculated with Eq. (6) systematically underestimate the experimental values. Likewise, the TEOP

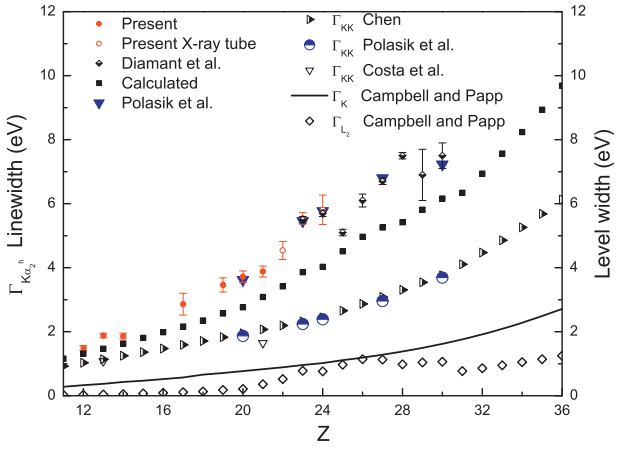

Fig. 7. Experimental OEOP linewidths and experimental data of Diamant et al. [59] as a function of *Z* (left *y*-axis). Plotted are also the values calculated with Eq. (6) and theoretical predictions of Polasik et al. [60]. On the right *y*-axis shown are the theoretical total level widths Γ_{KK} of Chen [36] and Costa et al. [51]. The Γ_K and Γ_{L_2} correspond, respectively, to the level widths *K* and L_2 recommended by Campbell and Papp [61].

Table 4
The $K\alpha^h$ to $K\alpha\alpha^h$ branching ratios for Mg, Al and Si. Also listed are different theoretical predictions. The $K\alpha^h$ rates from [53] are in the length gauge.

Z	Experiment	Theory
12	1838(258)	667 [65]
		928 [56]
		2417 [57,53]
13	2115(403)	758 [65]
		686 [68]
		999 [56]
		2617 [57,53]
		2359 [57,53][a]
14	2610(370)	833 [65]
		1126 [56]
		3007 [57,53]

[a] $K\alpha\alpha^h$ rates include the coupling of the initial and final state vacancies with the 3*p* electron.

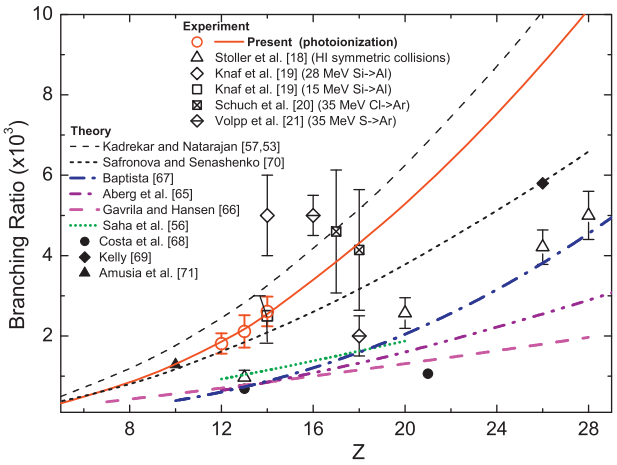

Fig. 8. $K\alpha^h$ to $K\alpha\alpha^h$ branching ratios for Mg, Al and Si (open circles) together with theoretical predictions as a function of the atomic number *Z*. The plots correspond to power-law fits to the data sets, whereas the solid line represents a Z^2-dependence. Experimental results from HI collision experiments are also shown for comparison.

linewidths are found to be ~1.6 times larger than those corresponding to the sum of the initial and final state widths given by Eq. (7). For Ne, on the other hand, the measured width of the Auger *KK-KLL* hypersatellite of 1.0(1) eV [14] is consistent with the sum $\Gamma_{KK}+\Gamma_K+2\Gamma_L$ of 1.08 eV. Recently a new approach based on elaborate Multi-Configuration-Dirac-Fock (MCDF) calculations and taking into account the influence of the effect of open-valence configuration and the outer-shell ionization and excitation was proposed to resolve the discrepancies [60]. Indeed, for selected elements in the $20 \le Z \le 30$ range, theoretical predictions of the effective $\Gamma_{K\alpha^h}$ linewidths were found to be in good agreement with the experiment (see Fig. 7). Thus, it can be concluded that an account of non-lifetime broadening effects such as the complex multiplet structure of the X-ray spectra resulting from the multi-configuration states and multiple-vacancies, the solid-state effects, and also to the multiplet splitting due the exchange interaction between the core-holes and the incomplete valence-shells in the theoretical X-ray spectra is prerequisite for comparison with experiment. On the theoretical side, calculations for lower *Z* elements and $\Gamma_{K\alpha\alpha^h}$ transitions are certainly called for. On the experimental side, measurements of TEOP transitions by means of high energy resolution X-ray spectroscopy techniques are also needed.

3.2.2. *One-electron one-photon to two-electron one-photon branching ratios*

The obtained mean values of the branching ratios are summarized in Table 4 and plotted in Fig. 8 along with data from heavy-ion collision experiments [17–21], and the *Z*-dependent trends of different theoretical approaches. To determine the branching ratios (BR) the following expression was employed:

$$BR = \frac{I^r}{I^{K\alpha\alpha^h}} \frac{\sigma_{KK}}{\sigma_K^r} \frac{n}{n^r} \frac{\omega_{KK}}{\omega_K^r} F_{exp}, \qquad (8)$$

where $I^{K\alpha\alpha^h}$ and I^r stand for the intensities of the $K\alpha\alpha^h$ and the close-lying reference *K* X-ray diagram transitions, respectively. σ_{KK} and σ_K^r are the double- and single-*K*-shell photoionization cross sections, ω_{KK} and ω_K^r are the fluorescence yields for the double- and single-hole states, and *n* and n^r denote the number of atoms per unit volume. F_{exp} is the experimental correction factor accounting for the relative differences in the photon flux, crystal reflectivity, detector efficiency, transmission of polycapillary optics, self-absorption, and relative transition probabilities of the *K*-shell emission lines. For ω_K^r, values from Ref. [64] were adopted, and for self-consistency those of ω_{KK} were rescaled accordingly from the ω_{KK}/ω_K ratios [2]. In our approach we took advantage of the well known values of the single [37] and the double [2] *K*-shell photoionization cross sections. For each element two reference *K* X-ray transitions were used to deduce the BR, i.e., for Mg the Cl $K\alpha$ of NaCl and KCl samples, for Al the K $K\alpha$ and Cl $K\alpha$ of KCl, and for Si the Sc $K\alpha$ and K $K\beta$. The BR values for Mg of 1880(373) and 1800(357), Al of 2040(541) and 2208(605), and Si of 2625(512) and 2594(536), were found to be consistent within the experimental uncertainties.

Since the two-electron one-photon radiative decay corresponds to a transition between correlated multi-electron initial and final atomic states, the transition rates are very sensitive to an accurate theoretical treatment of the electron inter- and intra-shell interactions. Indeed, the available predictions for the branching ratios show important differences (see Fig. 8). The predictions of Åberg et al. [65], Gavrila and Hansen [66], Baptista [67], Costa et al. [68], and Saha et al. [56] underestimate our experimental branching ratios. The BR values compare best to the most recent relativistic configuration interaction (RCI) calculations of Kadrekar and Natarajan [57,53] and to the many-body perturbation theory predictions [69–71]. Noteworthy is the good agreement of the RCI calculations [57,53] with the experimental branching ratio for Al when the coupling between the inner-shell vacancies and the outer incomplete subshells is included. The reported results give an important point of comparison for different theoretical models that address the many-body problem and demonstrate the potential of the TEOP radiative decay of *K*-shell hollow atoms to unravel electron correlations.

4. Concluding remarks and outlook

Understanding electron–electron interactions is not only one of the key issues of atomic physics, but is also important for an accurate theoretical description of complex systems and processes in the fields of physics and chemistry. Yet, on the theoretical side, an exact treatment of electron interactions in many-electron systems still represents a formidable challenge. Single-photon double ionization process producing core–shell hollow atoms and molecules [72,73] is a growing field, and the possibility to investigate experimentally ultrafast electron dynamics within atoms with XFELs opens new exploration routes [74–77]. Young et al. [3] reported on hollow Ne atoms created through a rapid photoejection of inner-shell electrons in an ultra-intense XFEL beam and the intensity-induced X-ray transparency, while the non-linear atomic response to intense X-ray pulses was reported by Doumy et al. [78]. These studies were performed by means of Auger and photoelectron spectroscopy. New aspects of hollow atom formation and decay such as X-ray emission from resonantly pumped double-hole *K*-shell states of Al were observed by Vinko et al. [79].

High resolution X-ray emission spectroscopy experiments investigating the dynamics of formation of hollow atom multi-vacancy states in multi-photon absorption and the following electron relaxation and rearrangement processes induced by ultra-intense X-ray pulses are also planned.

Acknowledgements

The authors acknowledge the financial support of the Swiss National Science Foundation and the ESRF.

References

[1] J. Hoszowska, et al., Phys. Rev. Lett. 102 (2009) 073006.
[2] J. Hoszowska, et al., Phys. Rev. A. 82 (2010) 063408.
[3] L. Young, et al., Nature (London) 466 (2010) 56.
[4] T. Åberg, Phys. Rev. A 56 (1967) 35.
[5] T.A. Carlson, M.O. Krause, Phys. Rev. 140 (1965) 1057.
[6] T.A. Carlson, J.C.W. Nestor, Phys. Rev. A 8 (1973) 2887.
[7] K.I. Hino, T. Ishihara, F. Shimizu, N. Toshima, J.H. McGuire, Phys. Rev. A 48 (1993) 1271.
[8] T. Schneider, P. Chocian, J.M. Rost, Phys. Rev. Lett. 89 (2002) 073002.
[9] T. Schneider, J.-M. Rost, Phys. Rev. A 67 (2003) 062704.
[10] A.S. Kheifets, J. Phys. B: At. Mol. Opt. Phys. 34 (2001) L247.
[11] A.I. Mikhailov, et al., Phys. Rev. A 69 (2004) 032703.
[12] E.P. Kanter, et al., Phys. Rev. A 73 (2006) 022708.
[13] S. Huotari, et al., Phys. Rev. Lett. 101 (2008) 043001.
[14] S.H. Southworth, et al., Phys. Rev. A 67 (2003) 062712.
[15] W. Heisenberg, Z. Phys. 32 (1925) 841.
[16] W. Wólfli, et al., Phys. Rev. Lett. 35 (1975) 656.
[17] A.R. Knudson, et al., Phys. Rev. Lett. 37 (1976) 679.
[18] C. Stoller, et al., Phys. Rev. A 15 (1977) 990.
[19] B. Knaf, G. Presser, J. Stähler, Phys. Lett. A 60 (1977) 106.
[20] R. Schuch, G. Gauker, H. Schmidt-Böcking, Z. Phys. A 250 (1979) 19.
[21] J. Volpp, et al., J. Phys. B: At. Mol. Opt. Phys. 12 (1979) L325.
[22] R. Diamant, S. Huotari, K. Hämälä inen, C.C. Kao, M. Deutsch, Phys. Rev. A 62 (2000) 052519.
[23] J. Hoszowska, et al., Phys. Rev. Lett. 107 (2011) 053001.
[24] V. Afrasimov, et al., JETP Lett. 21 (1975) 249.
[25] A.C. Hudson, W.C. Stolte, D.W. Lindle, Rev. Sci. Instrum. 78 (2007) 053101.
[26] L. Journel, et al., Rev. Sci. Instrum. 80 (2009) 093105.
[27] D. Sokaras, et al., Rev. Sci. Instrum. 83 (2012) 043112.
[28] M. Kavčič, et al., Rev. Sci. Instrum. 83 (2012) 033113.
[29] J. Hoszowska, J.-Cl. Dousse, J. Kern, C. Rhême, Nucl. Instrum. Methods Phys. Res. A 376 (1996) 129.
[30] B.A. Mattern, et al., Rev. Sci. Instrum. 83 (2012) 023901.
[31] J. Szlachetko, et al., J. Synchrotron Radiat. 17 (2010) 400.
[32] J. Szlachetko, et al., Rev. Sci. Instrum. 78 (2007) 093102.
[33] F. Bloch, P.A. Ross, Phys. Rev. 47 (1935) 884.
[34] T. Åberg, J. Utriainen, Phys. Rev. Lett. 22 (1969) 1346.
[35] R.D. Deslattes, et al., Rev. Mod. Phys. 75 (2003) 35.
[36] M.H. Chen, Phys. Rev. A 44 (1991) 239.
[37] http://www.nist.gov/pml/data/xcom/
[38] M. Oura, et al., J. Phys. B: At. Mol. Opt. Phys. 35 (2002) 3847.
[39] T. Pattard, T. Schneider, J.M. Rost, J. Phys. B: At. Mol. Opt. Phys. 36 (2003) L189.
[40] J.A.R. Samson, et al., Phys. Rev. A 57 (1998) 1906.
[41] A.S. Kheifets, D.V. Fursa, I. Bray, Phys. Rev. A 80 (2009) 063413.
[42] A.S. Kheifets, I. Bray, J. Hoszowska, Phys. Rev. A 79 (2009) 042504.
[43] J. Colgan, M.S. Pindzola, F. Robicheaux, J. Phys. B: At. Mol. Opt. Phys. 34 (2001) L457.
[44] J.A.R. Samson, Phys. Rev. Lett. 65 (1990) 2861.
[45] T. Pattard, J. Burgdörfer, Phys. Rev. A 64 (2001) 042720.
[46] T.D. Thomas, Phys. Rev. Lett. 52 (1984) 417.
[47] D.M. Mitnik, J.E. Miraglia, J. Phys. B: At. Mol. Opt. Phys. 38 (2005) 3325.
[48] R.C. Forrey, H.R. Sadeghpour, J.D. Baker, J.D. Morgan, A. Dalgarno, Phys. Rev. A 51 (1995) 2112.
[49] K. Aichele, et al., J. Phys. B: At. Mol. Opt. Phys. 31 (1998) 2369.
[50] T. Pattard, J. Phys. B: At. Mol. Opt. Phys. 35 (2003) L207.
[51] A.M. Costa, M.C. Martins, J.P. Santos, P. Indelicato, F. Parente, J. Phys. B: At. Mol. Opt. Phys. 40 (2007) 57.
[52] M.C. Martins, A.M. Costa, J.P. Santos, F. Parente, P. Indelicato, J. Phys. B: At. Mol. Opt. Phys. 37 (2004) 3785.
[53] L. Natarajan, Phys. Rev. A 78 (2008) 052505.
[54] E. Mikkola, O. Keski-Rahkonen, R. Kuoppala, Phys. Scripta 19 (1979) 29.
[55] O. Keski-Rahkonen, J. Saijonmaa, M. Suvanen, A. Servomaa, Phys. Scripta 16 (1977) 105.
[56] J.K. Saha, T.K. Mukherjee, S. Fritzsche, P.K. Mukherjee, Phys. Lett. A 373 (1932) 252.
[57] R. Kadrekar, L. Natarajan, J. Phys. B: At. Mol. Opt. Phys. 43 (2010) 155001.
[58] M. Kavčič, K. Tökési, Phys. Rev. A 72 (2005) 062704.
[59] R. Diamant, et al., Phys. Rev. A 79 (2009) 062511.
[60] M. Polasik, et al., Phys. Rev. Lett. 107 (2011) 073001.
[61] J.L. Campbell, T. Papp, At. Data Nucl. Data Tables 77 (2001) 1.
[62] F.P. Larkins, J. Phys. B 4 (1971) L29.
[63] D.F. Anagnostopoulos, J. Phys. B 28 (1995) 47.
[64] W. Bambynek, Proceedings of the X84 International Conference on X-ray and Inner Shell Processes, Leipzig, 1984.
[65] T. Åberg, K.A. Jamison, P. Richard, Phys. Rev. Lett. 37 (1976) 63.
[66] M. Gavrila, J.E. Hansen, J. Phys. B: At. Mol. Opt. Phys. 11 (1978) 1353.
[67] G.B. Baptista, J. Phys. B: At. Mol. Opt. Phys. 17 (1984) 2177.
[68] A.M. Costa, M.C. Martins, J.P. Santos, P. Indelicato, F. Parente, J. Phys. B: At. Mol. Opt. Phys. 39 (2006) 2355.
[69] H.P. Kelly, Phys. Rev. Lett. 37 (1976) 386.
[70] U.I. Safranova, V.S. Senashenko, J. Phys. B: At. Mol. Opt. Phys. 10 (1977) L271.
[71] M.Y. Amusia, L.S. Lee, A.N. Zinoviev, Phys. Lett. A 60 (1977) 300.
[72] J. Eland, et al., Phys. Rev. Lett. 105 (2010) 213005.
[73] P. Lablanquie, et al., Phys. Rev. Lett. 107 (2011) 193004.
[74] J.P. Cryan, et al., Phys. Rev. Lett. 105 (2010) 083004.
[75] L. Fang, et al., Phys. Rev. Lett. 105 (2010) 083005.
[76] N. Berrah, et al., Proc. Natl. Acad. Sci. U.S.A. 108 (2011) 16912.
[77] P. Salén, et al., Phys. Rev. Lett. 108 (2012) 153003.
[78] D. Doumy, et al., Phys. Rev. Lett. 106 (2011) 083002.
[79] S.M. Vinko, et al., Nature (London) 482 (2012) 56.